

Gradient-based Optimization of Submerged Composite Hydrofoils with Flutter and Ventilation Constraints

by

Galen W. Ng
nggw@umich.edu

Excerpt from a dissertation submitted in partial fulfillment
of the requirements for the degree of
Doctor of Philosophy
(Naval Architecture & Marine Engineering and Scientific Computing)
in the University of Michigan
2025

Doctoral Advisor:

Professor Joaquim R. R. A. Martins
jrram@umich.edu
<https://mdolab.engin.umich.edu/>

ABSTRACT

Composite materials enable hydrofoil designers to exploit material anisotropy for hydroelastic tailoring, improving hydrodynamic and structural efficiency, for example, through drag reduction and optimal load distribution. However, composite hydrofoils are limited by several constraints, two major ones addressed in this work are flutter instability and ventilation inception. Current methods for design optimization of hydrofoils consider only static hydroelasticity and neglect the system dynamics. This work presents a methodology for design optimization for a cantilevered composite hydrofoil considering flutter and ventilation constraints. The hydrofoil is modeled as a composite beam for the structure and as a lifting line for the hydrodynamics. A frequency-domain approach is used for the unsteady analysis. A gradient-based optimization algorithm drives the design iterations because these algorithms require fewer function evaluations than gradient-free methods to find an optimum. We compute gradients of functions of interest using methods that scale independently of the number of design variables. We conduct several design optimization studies using the constraints. Design studies demonstrate that flutter constraints are essential—static-only optimization produces flutter-susceptible designs. Including flutter constraints incurs drag penalties, primarily from parasitic drag because the optimizer thickens the structure to suppress flutter. Ventilation constraints limit minimum section chord and maintain section lift coefficient below critical inception values. The framework presented is a valuable tool for the rapid preliminary design of high-performance composite hydrofoils—especially when flutter and ventilation are of concern—with various applications to rudders, lifting foils, struts, propulsors, turbines, etc..

Introduction

Numerical optimization can accelerate the design of hydrofoils by attaching an optimization algorithm to a computational model of a hydrofoil and letting the computer do the design iterations a naval architect would normally do manually. In the hydrofoil optimization procedure, there will be an objective function describing the performance of the foil, design variables, and constraints. Typically, there are more design variables than there are objectives and constraints. Gradient-based optimization algorithms scale better than gradient-free algorithms when there are many design variables, so we prefer gradient-based methods to reduce computational cost.

Most hydrofoil designs focus on steady-state performance [24, 50, 63, 66, 75]. This type of analysis might be adequate for metallic structures, but recent research [3, 4, 81, 83] shows that the dynamic hydroelastic performance is also an important consideration for streamlined, lightweight, flexible, marine structures subject to high loading. Excessive flow-induced vibrations, noise, dynamic load amplifications (i.e., a large amplification factor of a fluctuating load), and accelerated fatigue can be caused by many system dynamics phenomena. Some examples include lock-in phenomena [12, Sec. 3.3], classical resonance [76, Ch. 1], parametric resonance [19], frequency coalescence [86, 87], and hydroelastic instabilities such as flutter and limit-cycle oscillations. Flutter instability is one of the main phenomena we address in this work. Flutter is a self-excited, dynamic instability that occurs at some critical speed when the system damping of one of the modes is equal to or less than zero, resulting in sustained or growing oscillations at fixed frequency.

A unique aspect of composite hydrofoils is that the solid-to-fluid added mass ratio (μ) is of the order 1/2 or less whereas aircraft wings μ may be of order 50 or more [36]. Metallic hydrofoils have a higher μ compared to composite ones. Low μ systems, such as marine and biomedical devices, tend to have lower instability speeds [16–18] because of the greater relative importance of fluid dynamic loads. The governing instability modes typically differ between airfoils and hydrofoils because of the relative contribution of fluid loads, so hydrofoils are usually governed by static divergence. In contrast, aerospace structures normally experience flutter [3, 16]. The physics of lower μ foils are further complicated by viscous effects that alter the center of pressure location and resulting fluid-structure interaction. Viscous models become more important for accurate instability speed prediction as μ decreases because inviscid assumptions tend to be non-conservative at low

μ [17, 18]. Composites are relatively new to marine lifting surface design, so the combined influence of low structural density and material anisotropy on dynamics is not as well-understood.

Before the 1950s, hydroelastic flutter was thought to be highly unlikely in contrast to aeroelastic flutter, because μ was low and the reduced frequencies $k = \omega b/U_\infty$ were high for the slow ship speeds at the time [36]. The theoretical flutter prediction work at the time was limited to 2D incompressible flow, and it suggested that below some critical μ , flutter was not possible except for sweptback surfaces [80]. However, it was experimentally shown in the 1970s as part of the US Navy's Hydrofoil Development Program that hydroelastic flutter could occur on subcavitating hydrofoils. These laboratory experiments and accompanying theoretical work on hydrofoil strut systems made of lightweight isotropic structures showed that dynamic instabilities were problematic [7–10, 52]. This general understanding of mass ratio effects on flutter speeds is summarized in Figure 1. Nondimensionalization of flutter speed U_F in Figure 1 is by the semichord b and first torsion frequency ω_α . This work uses improved computational models that can predict flutter at low μ , thus resolving the discrepancies that previously were the subject of much debate.

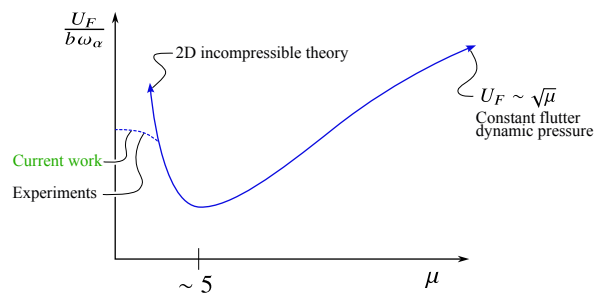


Figure 1: The nondimensional flutter speed versus mass ratio shows disagreement between 2D theory and experiments on flutter speeds of hydrofoils at low μ . We use improved models that predict finite flutter speeds in the low μ range.

The theoretical deficiency was the disregard of finite wing effects on the unsteady hydrodynamics. Yates [79] developed a modified strip analysis to account for finite wing effects. Yates [80] applied this method to low mass ratio hydrofoils to predict finite flutter speeds of unswept wings. This led to the important conclusion that considering finite wing effects, though more compute intensive than 2D calculations, is necessary for predicting flutter at low mass ratios. Dowell [21, Sec. 6.3] says that flutter for small μ is still a source a controversy and some say the cause of flutter for low μ systems is

viscous effects [2] or the chordwise flexibility. There is a wealth of research from that timeframe on hydrofoil flutter as summarized by Abramson [2], most likely prompted by interest in hydrofoil craft and the Navy’s pursuit of 100 kts for their surface vessels. Examples include the HS DENISON designed by Grumman and the US Navy FRESH-1 designed by Boeing¹.

Flutter is still a present problem that has resurfaced in high-performance composite vessels. As a modern example, flutter on racing yacht keels was first reported in 2004 on the IMOCA 60 yachts in two separate instances. The first was the Poujoulat–Armorlux during the transatlantic race, where the skipper lost their keel and capsized the vessel. The Sill also experienced flutter [6]. Both vessels had canting composite keel fins, so the mounting joint had flexibility. More recently, the rudder of Ineos Britannia’s AC40 showed an oscillatory phenomenon that led to the destruction of the rudder and loss of control of the towed vessel². We are unsure of the composition of their rudder, but it may have been partially composite.

Computing power has significantly increased since the 1970s so the older flutter analysis methods that were shown to have decent agreement to experiments are now quick enough for them to be used in design optimization where several analyses are required. Methods to consider flutter constraints in gradient-based design optimization have also been developed for aerospace applications [29, 38, 40], but they have not been applied to hydrofoil optimization.

Another unique challenge to hydrofoil design is ventilation. Ventilation is the entrainment of a noncondensable gas. It usually incepts when the local pressure drops below the pressure of an impinging noncondensable gas (such as air from the atmosphere) and when a continuous path of air ingress is available [82]. As such, ventilation is a significant challenge for surface craft, especially surface-piercing foils, struts, or propellers because the atmosphere has a shorter path into low pressure regions. There have been several studies characterizing the conditions under which ventilation inception is probable [20, 32, 85–87]. There have not been any gradient-based design optimization studies where a ventilation inception constraint was used.

This work achieves two objectives: (1) we develop a gradient-based optimization workflow for composite hydrofoils considering flutter and ventilation constraints and (2) we investigate the impact of considering flutter and ventilation on design optimization of minimum drag composite hydrofoils. Neither of these have been explored in the published literature.

¹This vessel experienced a high-speed capsiz at 70 kts in 1963

²[youtube.com/watch?v=6VPslDzbCJA](https://www.youtube.com/watch?v=6VPslDzbCJA)

Methodology

The core physics solver in this work is called DC-Foil.jl [55]. It is a reduced-order model for the dynamic analysis of composite hydrofoils. Ng et al. [55] discusses the theoretical details. In summary, the structure is modeled as a Vlasov composite beam, which is more accurate than classical Euler–Bernoulli beam theory for lower aspect ratios when the restrained warping effect (a.k.a. Vlasov effects [74]) impacts the torsional rigidity. The steady-state hydrodynamics are modeled using the nonlinear numerical lifting line of Phillips and Snyder [58] with improvements by Reid and Hunsaker [62]. The computation of unsteady hydrodynamic loads follow the modified strip analysis of Yates [79] that has been extended to consider sweep [11, Sec. 9.8].

The flutter solution is the p - k method commonly used in aeroelastic flutter predictions [33]. We employ a mode tracking algorithm [72] and a non-iterative root finding algorithm to solve for p [73]. Both features are necessary for robust and smooth flutter analysis to compute gradients of the flutter constraint [38, 39]. The nondimensional complex eigenvalue is $p = \xi + jk$, where ξ is nondimensional damping and k is the reduced frequency. By sweeping flow speed (U_∞), we find the point where $\xi > 0$ and an unstable solution arises; this is the critical instability speed. The instability is called flutter if $k > 0$ and static divergence if $k = 0$. Typically, we plot the evolution of p in the Argand plane and determine the stability based on where p is. The regions of stability are in Figure 2.

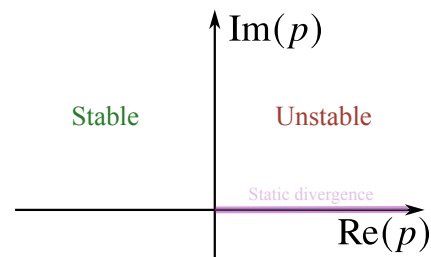


Figure 2: Plotting the evolution of eigenvalues p in the Argand plane across a speed sweep allows us to determine the hydroelastic stability.

Restructuring the solver architecture

To facilitate scalable and modular multidisciplinary design optimization, we restructured the code initially implemented by the authors [55] to use OpenMDAO [30]. OpenMDAO is an open-source Python and Julia package that uses the modular analysis and unified derivatives

(MAUD) mathematical architecture. There are a few basic reasons for this, which are: (1) to couple systems in a modular and scalable way that generalizes the multidisciplinary analysis (2) to make the computation of derivatives of two or more coupled systems easier, and (3) to facilitate the interfacing of the multidisciplinary model with optimizers. OpenMDAO's mathematical foundation is the unified derivatives equation (UDE) [35, 53], which generalizes analytic derivative methods. MAUD is powerful because it can handle both implicit and explicit forms of systems. An initial version of DCfoil had its own custom discrete adjoint for the static hydroelastic solution and algorithmic differentiation (AD) for the dynamic solver. However, now we structured the code to compute all partial derivatives needed by OpenMDAO to assemble the total derivative.

Because there are three solution modes in DCfoil and it is used in an optimization framework, we present an eXtended Design Structure Matrix (XDSM) diagram [48] to provide an overview of the current methodology in Figure 3. The other components in the optimization framework are the geometry parametrization modules [31, 42] and optimization module [78]. Off-diagonal blocks in Figure 3 show data flow. The iterative optimization algorithm used throughout this work is the constrained sequential quadratic programming (SQP) method in the optimizer called SNOPT [25–27]. SNOPT is a general purpose optimizer suitable for large-scale and general constrained nonlinear optimization problems. It is a gradient-based optimization algorithm that performs best when the functions are smooth and users provide gradients.

Part of restructuring DCfoil to work using OpenMDAO was separating the steady-state fluid and structural disciplines to use two separate residual equations

$$\mathbf{r}_s(\mathbf{u}) = \mathbf{0} \quad \text{structural discipline} \quad (1)$$

$$\mathbf{r}_f(\boldsymbol{\gamma}) = \mathbf{0} \quad \text{hydrodynamic discipline} \quad (2)$$

where the vector \mathbf{u} are the structural states and $\boldsymbol{\gamma}$ are the flow states. The static hydroelastic analysis is thus based on implicit forms. Tight coupling between the fluid and structural models is achieved through a load and displacement transfer scheme and a nonlinear block Gauss–Seidel (fixed-point iteration) scheme to converge the two systems of equations.

The dynamic hydroelastic analyses are in explicit forms that use the linearized quantities from the static equilibrium solution to compute the flutter and forced vibration response.

Drag build-up

For DCfoil to be used in design optimization, we need a simple model for predicting drag, since that is

our objective function. The following drag build-up is an extension of our previous work [56], but with a few modifications.

A steady-state drag build-up model must consider parasitic drag (D_p) and drag due to lift. Drag due to lift is not the same as lift-induced drag [44]. In equation form, total calm-water drag (not considering multiphase flow) is

$$D = D_p + \underbrace{\frac{L^2}{\frac{1}{2}\rho U_\infty^2 \pi \tilde{s}^2 e}}_{\text{drag due to lift}} \quad (3)$$

where

$$D_p = D_{\text{fric}} + D_{\text{form}} + D_{\text{int}} + D_{\text{spray}}, \quad (4)$$

and e is the Oswald efficiency factor. Our model for the drag due to lift consists of the lift-induced drag (D_i) and wave-pattern drag (D_w). The parasitic drag—everything that is not drag due to lift—consists of interference (D_{int}), spray (D_{spray}), skin friction (D_{fric}), and form drag (D_{form}). Because of the geometry we are studying, we omit the spray and interference drags. To supplement the equation form of total drag, Figure 4 hierarchically categorizes the drag components and typical nomenclature used to describe calm-water drag. We do not consider added resistance due to motions in waves.

The lift-induced drag is computed directly by the lifting line method. It is the sum of the streamwise force components from the vectorized Kutta–Joukowski theorem [46, 88], which is

$$d\vec{F}_i = \rho \Gamma_i \vec{U}_i \times d\vec{\ell}_i \quad \text{for } i = 1, \dots, N_v \quad (5)$$

for N_v abutted horseshoe vortices. The vortex strengths are Γ_i , the local induced velocities are \vec{U}_i , and the spatial vector along the bound vortex is $d\vec{\ell}_i$. The sum of $d\vec{F}_i$ in the streamwise direction is the lift-induced drag. Further details are presented by Reid and Hunsaker [62].

Due to lifting and thickness effects, the foil generates surface waves, which adds a component called wave drag. The lifting effect on the generated waves tends to be more important. In 2D, wave drag goes to zero at very high depth-based Froude numbers $Fn_h = U_\infty/\sqrt{gh}$ [23, Ch. 6]. In the case of 3D flow, the 2D behavior is that of the transverse waves. The divergent waves still contribute to wave drag regardless of how high Fn_h is. The wave drag prediction is given by Breslin [14] assuming an elliptic lift distribution and linearized potential flow. The expression for total inviscid drag (valid for

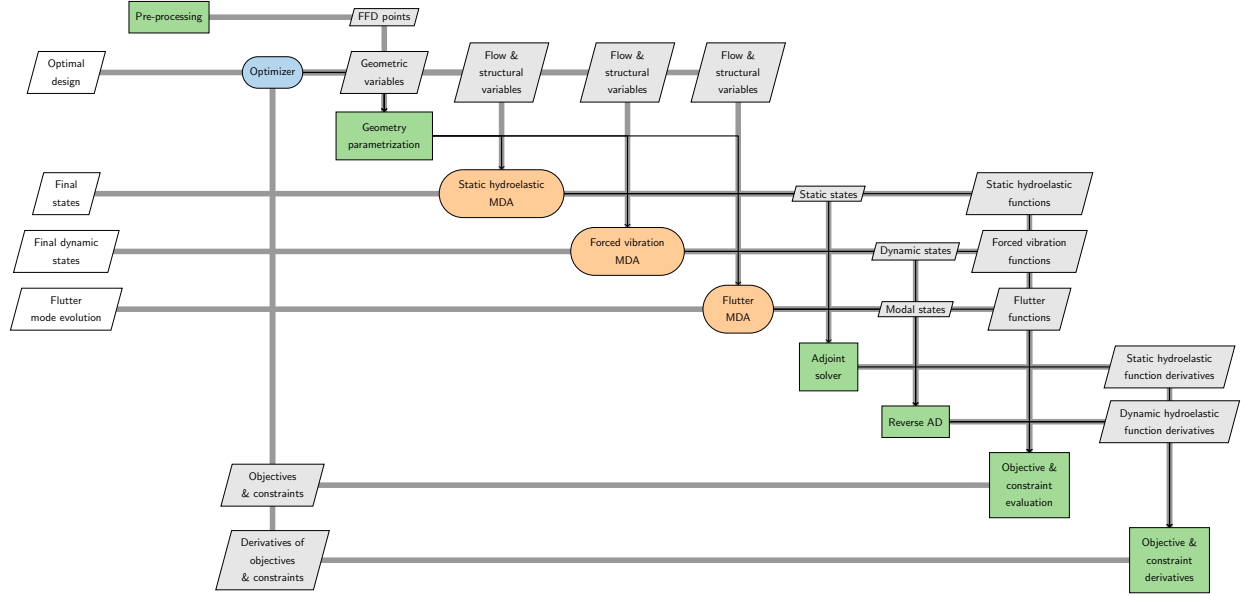


Figure 3: Optimization framework XDSM diagram [48] using the reduced-order hydroelasticity model. Main diagonal blocks in orange are the core analyses that have their own solvers. Green boxes show analyses using information passed to them. Off-diagonal blocks are variables and arrows denote the direction these variables flow. The optimizer in the blue circle drives this whole process. White boxes are converged results. The reader is referred to Lambe and Martins [48] for in-depth description of terminology.

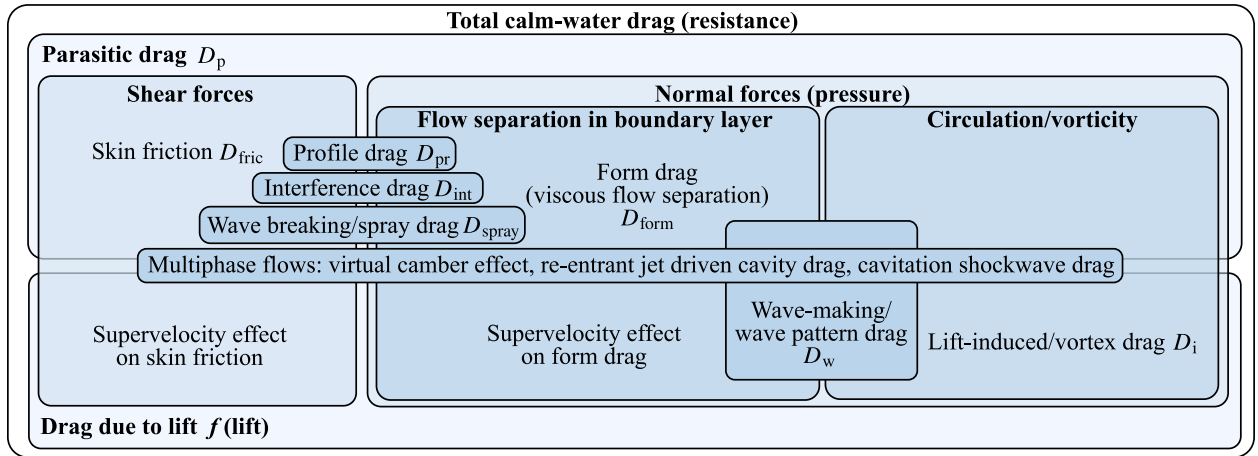


Figure 4: Sources of hydrodynamic drag in calm-water.

any Fn)

where

$$\frac{C_{D_{inv}}}{C_L^2} = \frac{1}{\pi \mathcal{R}} - \frac{\sigma(\lambda)}{\pi \mathcal{R}} + \frac{8}{\pi \mathcal{R}} \int_0^{\pi/2} \frac{J_1^2\left(\frac{g}{U_\infty^2} \frac{s}{2} \sec^2 \theta \sin \theta\right) e^{-\frac{2 \sec^2 \theta}{Fn_h^2}}}{\sin^2 \theta \cos \theta} d\theta$$

$$\begin{aligned} \sigma(\lambda) &= 1 - \frac{4}{\pi} \lambda \sqrt{1 + \lambda^2} \\ &\left[K\left(\frac{1}{\sqrt{1 + \lambda^2}}\right) - E\left(\frac{1}{\sqrt{1 + \lambda^2}}\right) \right] \\ \lambda &= \frac{2h}{s}. \end{aligned}$$

The depth is h , the full span of the hydrofoil is \tilde{s} , and the acceleration due to gravity is g . The functions K and E are complete elliptic integrals of the first and second kind [1, Ch. 17]. The function J_1 is the Bessel function of the first kind of order 1 [1, Ch. 9]. The first term in the inviscid drag expression is the lift-induced drag. The term $\sigma(\lambda)$ is the well-known Prandtl biplane function [59]. These particular closed-form expressions for $\sigma(\lambda)$ from [23, Ch. 6] assume elliptical circulation distributions. To not double count the lift-induced drag in an unbounded fluid, we only take the last two terms from Breslin's expression in our drag build-up. The wave drag prediction compares well to experimental measurements by Wadlin et al. [77].

The profile drag (skin friction plus form) at hydrofoil sections assumes a flat-plate estimate with form factor corrections. The friction drag is estimated via the ITTC 1957 line

$$C_f = \frac{D_{\text{fric}}}{\frac{1}{2}\rho U_\infty^2 \text{WSA}} = \frac{0.075}{(\log_{10}(Re) - 2.0)^2}, \quad (6)$$

where WSA is wetted surface area. The equation is an empirical formula for skin friction of naked ship hulls assuming turbulent flow [15]. The empirical form factor $(1+k)$ is determined from Torenbeek [69] for a subsonic wing

$$1+k = 1 + 2.7 \left(\frac{t}{c}\right) + 100 \left(\frac{t}{c}\right)^4, \quad (7)$$

where the first term with thickness captures the increased skin friction from thickness effects and the quartic term accounts for flow separation drag. This equation misses the lifting effects on the profile drag, sometimes referred to as the "supercritical" effect [61, Sec. 12.5.5], which increases the skin friction and form drag. Profile drag is then

$$D_{\text{pr}} = (1+k)D_{\text{fric}}. \quad (8)$$

Consideration of free surface effects

Following Besch and Liu [7, 8], Liu and Besch [52], we use a high-speed, high-frequency limit correction for the free surface effect since these are the conditions where flutter is likely. Most important problems in hydroelastic stability will usually occur at high Fn . The linearized free surface boundary condition in the frequency domain is

$$-\frac{\omega^2}{g}\varphi + \frac{\partial\varphi}{\partial z} = 0 \text{ on } z = 0 \quad (9)$$

where φ are the perturbation potentials [47, Ch. IX]. For $\omega \rightarrow \infty$, the result is $\varphi = 0$ on the free surface, which

leads to the antisymmetry boundary condition [54, Sec. 6.17], analogous to a biplane in aerodynamics.

Faltinsen [23, Sec. 6.8.2] remarks that correcting the sectional vorticity and combining with a lifting line solution for the downwash is an accurate approximation to 3D free surface effects at the high Fn_h limit. When the circulation distribution is elliptical, the downwash is constant and so this 2D free surface correction generalizes well to 3D. The theoretical 2D free surface correction for $Fn_h \rightarrow \infty$ originally presented by Wadlin et al. [77] is

$$\frac{\gamma_{2D}(\frac{h}{c})}{\gamma_{2D}(\frac{h}{c} = \infty)} = \frac{1 + 16(h/c)^2}{2 + 16(h/c)^2} \quad (10)$$

which would be applied at each spanwise section. This 2D correction approach is faster to compute than modeling the entire negative image, but this model breaks down for non-elliptic loading. This approach compares well with experiments by Van Walree [71] for rectangular foils with $\mathcal{R} = 6$ at higher Fn_h . Ng et al. [56] followed this as have others in similar manners [37, 68], and the approach is used here for the inner airfoil solve of the lifting line. Thiart [68] generalized this 2D free surface correction of the lifting line to work with non-elliptic loads and arbitrary Fn_h .

The modified c_{ℓ_α} affects only the quasi-steady forces (i.e., fluid damping and fluid de-stiffening). It does not correct the added mass. Even so, this is still not to be considered accurate because the frequency-dependent transfer functions on the circulatory loads (Theodorsen and Sears functions) are the same. Theodorsen [67] and Sears [64] original derivations assumed radiation conditions in the farfield, so by continuing with the unmodified circulation functions here, we are neglecting how free-surface proximity changes the induced circulatory forces from wake vorticity. These neglected effects are frequency-dependent, so for flutter occurring at higher reduced frequencies, this may be an acceptable approximation.

Fluid added mass for objects near a free surface is quite complicated, especially if using the fully nonlinear free surface condition [13, Sec. 3.8]. The added mass calculation in potential theory depends on shape, depth, frequency of motion, direction of motion, and forward speed. The majority of modern approaches use numerical methods to compute the added mass, which is more compute intensive than analytic formulae. Besch and Liu [7], Liu and Besch [52] and Besch and Liu [8] applied empirical spanwise correction factors p to 2D values that enforced the added mass to be zero at the free surface for their surface-piercing foil, which is applicable at high reduced frequencies. They compared recently with experimental measurements by Baird et al.

[5]. Their correction factor for the i th strip is

$$p_i = \frac{\mathcal{R}_i}{\sqrt{1 + \mathcal{R}_i^2}} \quad (11)$$

where \mathcal{R}_i is the local aspect ratio of the i th strip using the submerged span of the local position in the case of surface-piercing bodies. The midspan of the submerged portion of the foil is a reflecting plane in the case of a submerged geometry with a free tip.

Constraints

The flutter constraint we use was first presented by Jonsson et al. [38]. It uses double Kreisselmeier–Steinhauser (KS) aggregation [43] on $\text{Re}(p)$: first for all dynamic pressures ($q = 1, \dots, N_q$), and then for all evaluated modes ($n = 1, \dots, N$). The result is the single constraint

$$g_{\text{flutter}} = \text{KS} [\text{KS} (\text{Re}(p_{n,q}))] \leq 0. \quad (12)$$

This flutter constraint is based on linearized theory and small amplitude deflections. It is adequate if nonlinear flow and structural effects are stabilizing. When the nonlinearities are stabilizing, this is called supercritical limit cycle oscillation (LCO). It is possible to have subcritical LCO where the nonlinearities are destabilizing, in which case, beyond small amplitude deflections, this flutter constraint is insufficient [28]. This constraint is adequate for preliminary design.

Damley-Strnad et al. [20] derived a semi-empirical ventilation criteria by fitting experimental data in the Fn_h - C_L space. In the context of strip theory, we can adapt their relation to

$$c_{\ell_{in}}(y) = \frac{1 - e^{-\sigma_v Fn_h(y)}}{\sqrt{Fn_h(y)}} \quad (13)$$

where $c_{\ell_{in}}$ is the sectional lift coefficient along the span at which ventilation incepts. To constrain ventilation, we set a design free surface cavitation number $\sigma_v^* = (p_{\text{atm}} - p_{\text{vap}}) / (\frac{1}{2} \rho U_\infty^2)$ that uses vapor pressure as the cavity pressure. If there were subatmospheric conditions, such as the experiments by Swales et al. [65] where they tested at $0.046 p_{\text{atm}}$, then the p_{atm} term in σ_v^* would be reduced, as would the predicted lift coefficient of inception.

To keep local lift coefficient below the inception lift coefficient, we evaluate the ventilation constraint everywhere along the span and apply a KS aggregation to find the smooth maximum.

$$g_{\text{vent}} = \text{KS} (c_{\ell,i} - c_{\ell_{in},i}) \leq 0 \quad (14)$$

Model setup

The geometry is a tapered 0.9 m semispan foil similar to the one studied by Ng et al. [57]. A schematic of the front view and top-down view are in Figure 5 and Figure 6, respectively. The fiber angle θ_f is measured from the midchord axis y' such that when there is a sweep angle Λ , there is a local set of axes ($x'y'z'$) from which θ_f is measured.

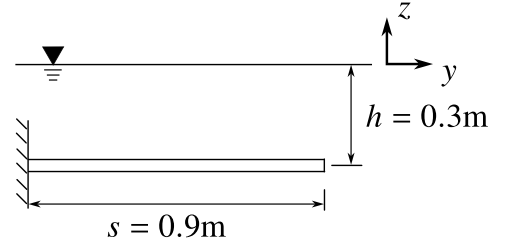


Figure 5: Front view

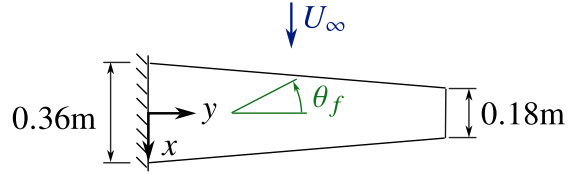


Figure 6: Planform view

For the contrived purposes of demonstrating the flutter constraint, we make a few settings. We use the material properties of a much softer polymer matrix composite (PMC) listed in Table 1. The baseline fiber angle is aligned towards the leading edge to induce some tip washout ($\theta_f = 15^\circ$). The distance from the elastic axis (e.a.) to the midchord is set to $ab = -0.0928b$ along the span based on experimental measurements by Young et al. [84] for a geometrically similar carbon fiber-reinforced plastic (CFRP) foil. We also set the static imbalance arm to be $x_\alpha b = 0.0928b$ along the span so the center of gravity is at the midchord. Furthermore, a 4 kg tip mass with a 2 kg-m^2 moment of inertia is placed 0.2 m aft of the e.a. Adding the tip mass is similar to bulb keels or podded propulsion. With these settings, the baseline foil has flutter instability very close to 25 m/s. The foil is discretized into 20 collocation points for the lifting line model and 10 nodes for the beam model. We assume seawater properties given in Table 2.

The DCfoil model is parametrized using leading edge (LE) and trailing edge (TE) coordinates embedded within a free-form deformation FFD volume shown in Figure 7.

Table 1: Polymer matrix composite properties. Subscript 1 and 3 are transverse to the fiber axes and subscript 2 is along the fiber length.

Solid density	ρ	1800	kg/m ³
Transverse Young's modulus	$E_1 = E_3$	4.47	GPa
Longitudinal Young's modulus	E_2	39.27	GPa
Shear modulus	$G_{12} = G_{23}$	1.30	GPa
Poisson's ratio	ν_{23}	0.25	–

Table 2: Flow constants

Atmospheric pressure	p_{atm}	101.3	kPa
Vapor pressure	p_{vap}	2.34	kPa
Dynamic viscosity	μ	1.12×10^{-3}	kg-m/s
Fluid density	ρ	1025	kg/m ³

We generate LE and TE coordinates for a full span foil and apply the FFD volume to the whole span even though we only work with a semispan during optimization. The reason is so that it would be easy to progress to full span optimizations in the future where we could consider leeway and heel angles. This does not significantly increase the computational load.

Optimization problem statement

We want to design a low-drag composite foil that is structurally sound and avoids ventilation and flutter. Table 3 summarizes the full optimization problem. We have constraints on lift, static tip deflection, ventilation, and flutter. We set the optimality and feasibility tolerances for SNOPT to 10^{-4} . Optimality tolerance quantifies the maximum complementarity gap (i.e., the degree of optimality) and is a measure of the tolerance on the Karush–Kuhn–Tucker (KKT) conditions [41, 45]. The KKT conditions are the foundation of gradient-based constrained optimization algorithms as they give the first-order constrained optimality conditions. The feasibility tolerance quantifies the nonlinear constraint violation. Linear constraints are satisfied at the quadratic problem level. We want both tolerances as close to zero as possible.

We design for three flow conditions representing an operating profile given in Table 4. Because planform area can vary, the reported C_L is based on the initial reference area. The speeds and loadings are based on Liao et al. [50], Ng et al. [57], but the depths are much lower to see the impact of free-surface proximity on design.

For the flutter speed sweep, the angle of attack is set to $\alpha_0 = 4^\circ$. Because the structural model is linear, the angle of attack will not significantly impact the flutter prediction. The speed sweep is from 5–25 m/s with an

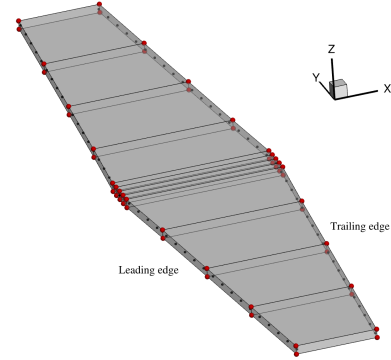


Figure 7: DCfoil leading edge and trailing edge mesh embedded within an free-form deformation (FFD) control volume (red dots are FFD control points).

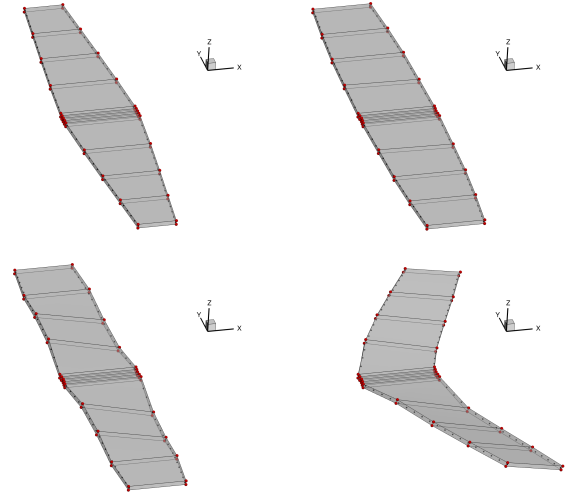


Figure 8: From left to right and top to bottom, the baseline geometry has span, taper, twist, and sweep progressively added so the final image shows all geometric design variables applied.

Table 3: Complete optimization problem statement.

	Symbol	Description	Lower	Upper	Units	Qty
minimize	$\sum_i^{\text{npts}} \text{wt}_i \times D$	Weighted drag			N	1
by varying	α_0	Root angle	-10	10	°	1
	θ_f	Equivalent laminate fiber angle	-30	30	°	1
	t/c	Thickness/chord ratio	9%	18%	–	10
	Λ	Sweep angle	0	30	°	1
	s	Hydrodynamic span	$s_0 - 0.1$	$s_0 + 0.1$	m	1
	TR	Taper ratio	0.5TR_0	1.4TR_0	–	1
	γ	Twist distribution	-10	10	°	4
		Total number of design variables				19
subject to	L	Lift constraint	L^*	L^*	–	npts
	g_{vent}	Ventilation constraint (Equation 14)	–	0	–	npts
	w_{tip}	Static tip bending constraint	–	5% initial semispan	m	1
	g_{flutter}	Flutter constraint (Equation 12 with $\rho_{\text{KS}} = 500$)	–	0	–	1
		Total number of constraints				8

upper limit on 25 m/s because there would be extensive cavitation or ventilation on the foils beyond this speed, so the fluid models and thus flutter predictions would not be accurate.

Results

There are three sets of optimizations. The first set are single point static optimizations. These are run with the free surface and added mass corrections on and off. There are a handful of published studies looking at the effects of free surface proximity on flutter behavior of subcavitating hydrofoils. Abramson [2] notes that flutter speed generally increases as a fully submerged foil nears the free surface, a conclusion that is supported by theoretical and numerical results. It is both conservative and practical to use classical theory, without consideration of a free-surface, for flutter analysis of fully submerged hydrofoils; this means it is valuable to consider free surface effects to avoid an overly conservative design. Abramson [2] notes that flutter in the single degree of freedom (DOF) of pitch is exacerbated by free-surface proximity, so it may be important in control surface design.

The second set of optimizations are single point static and dynamic optimizations. These single point optimizations use the ‘p3’ condition in Table 4.

The third set is the multipoint static and dynamic optimizations. We abbreviate the sets of results according to the names in Table 5. The baseline designs used in comparisons are all trimmed to match the lift constraint.

Single point optimizations

Table 6 summarizes all designs in this section.

Static only

After performing static hydroelastic optimization, we obtain the ‘opt1’ and ‘opt1-fs’ designs. These designs achieved around 13% drag reduction. The spanwise distributions of the ‘opt1’ and baseline composite foils are plotted in Figure 9.

The baseline produces too much lift inboard and violates the ventilation constraint. The consideration of the free surface has no significant impact on the static performance of the optimized design nor does it result in a different design for this particular flow condition. The angle of attack increases for ‘opt1-fs’ to match the lift constraint by a very small amount compared to ‘opt1’. Other parameters also vary just slightly, but the changes are so small that they could be attributed to the optimality and feasibility tolerances. Because of the negligible differences in all aspects, we omit it from Figure 9 for clarity.

For planar lifting surfaces where lift is the only constraint, the elliptical distribution of lift is the most hydrodynamically efficient because it gives the minimum lift-induced drag. Increasing the span also reduces lift-induced drag. The optimized foil increases its span to the upper bound. We have additional constraints that cause deviations from the ideal distribution, such as the tip bending constraint, which should favor inboard loading. The optimized foil displays a bell-like shape in its lift distribution in Figure 9 and thicker cross-sections towards the root to satisfy the tip bending constraint. This trades increased form drag for reduced lift-induced drag whilst satisfying the tip bending constraint.

When we say bell-like distribution, we do not mean the analytic bell-shaped distribution determined by Prandtl [60] because our problem is different.³ Prandtl [60] orig-

³Hunsaker and Phillips [34] gives the English translation of the

Table 4: Optimization design conditions.

Point ID	Condition	U_∞	h [m]	Fn_h	L^* [N]	C_L	σ_v^*	wt
p1	Top speed	24 m/s	0.3	14	14000	0.2	0.34	30 %
p2	Cruise	20 m/s	0.3	11.7	14500	0.3	0.48	60 %
p3	Maneuvering	17 m/s	0.3	9.9	21000	0.6	0.67	10 %
	Flutter envelope	5–25 m/s	0.3					

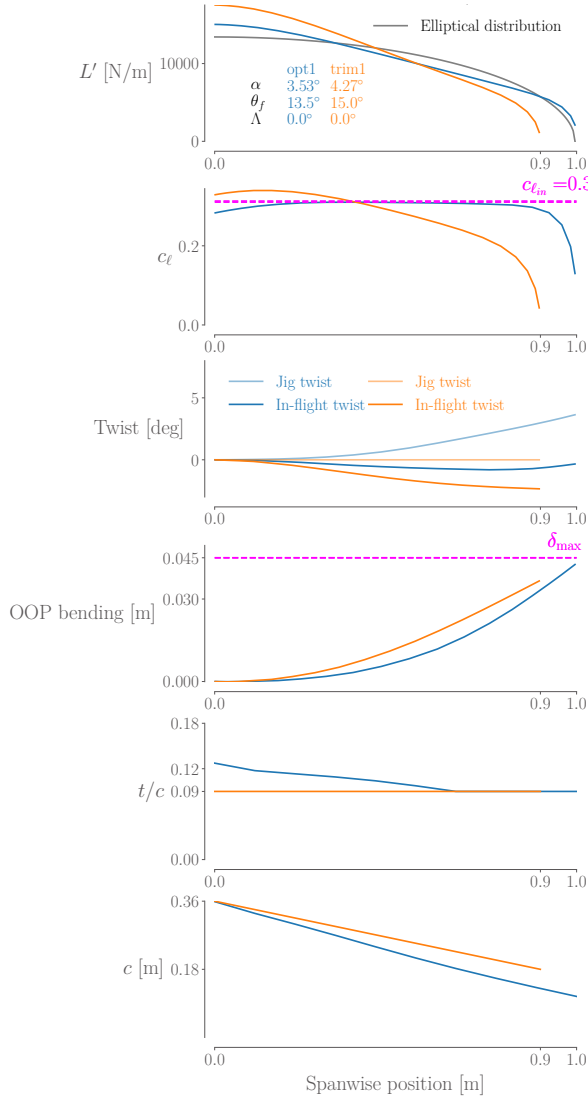


Figure 9: Spanwise attributes of the single point static optimized hydrofoil compared to the baseline (orange) at the 17 m/s condition.

Table 5: Optimization matrix. When there is a free surface model in the optimization, ‘-fs’ is appended to the name.

Name	Description
opt1	Single point static hydroelastic optimization
opt2	Single point static and dynamic hydroelastic optimization
opt3	Multipoint static and dynamic hydroelastic optimization

inally determined an analytic relation for a bell-shaped lift distribution that has the minimum lift-induced drag for a given lift and moment of inertia of the lift distribution (i.e., bending moment). Prandtl did not include parasitic drag in his calculations nor were there ventilation constraints that impact the minimum total drag design. This current work also has a structural model while Prandtl worked solely with an aerodynamic model.

Slightly positive fiber angles balance bending rigidity with hydroelastic washout from nose-down material bend-twist coupling. The jig twist is also tailored to consider this deflected shape. The ‘in-flight’ twist in Figure 9 remains near but slightly below 0° throughout most of the span before increasing slightly at the tip. The slight increase of twist near the tip helps fill out the c_l distribution subject to the ventilation constraint.

The interplay between the ventilation constraint and design variables has an impact on the distribution achievable. The semi-empirical ventilation constraint is analogous to a $c_{l_{\max}}$ constraint used in aerodynamic design. Nevertheless, this may be the first instance of its use in gradient-based design optimization. We see the optimized foils tailor their spanwise c_l distributions to remain below the critical value despite tapering. Tapering reduces skin friction drag but increases local c_l . If heel angles were considered, we would expect the distribution to follow a modified bounding $c_{l_{in}}$ envelope instead of the rooftop in this simpler study.

Table 6: Summary of single point optimized designs with percent differences in objective function relative to baseline

Parameter	opt2-fs	opt2	opt1-fs	opt1	Baseline	Units
Objective						
D	615 (-9.7%)	624 (-8.2%)	592 (-12.9%)	595 (-12.5%)	680	N
Design variables						
α_r	3.05	2.91	3.72	3.53	4.27	$^\circ$
θ_f	14.0	14.0	13.9	13.5	15	$^\circ$
t/c	See Figure 9	See Figure 16	Same as opt1	See Figure 9	9%	
Λ	6.8	6.8	0	0	0	$^\circ$
s	1.0	1.0	1.0	1.0	0.9	m
TR	0.92TR ₀	0.92TR ₀	0.6TR ₀	0.6TR ₀	TR ₀	
γ	See Figure 9	See Figure 16	Same as opt1	See Figure 9	0	$^\circ$

No sweep is present, which suggests it is not a critical design variable in this single point optimization. Sweep usually helps in multipoint optimization. Sweep alters lift distributions in a load-dependent way and can modify cavitation inception speed and susceptibility to structural failure such as shown in other works [49–51, 57]. Our reduced-order model will not capture the effect of sweep on cavitation inception speed, but it can capture the other effects. DCfoil can also capture the impact of sweep on flutter instability.

A drag breakdown in Figure 10 reveals where most of the performance gains are. The drag of the baseline design comes primarily from profile and lift-induced drag in nearly equal proportions; the wave-pattern drag is of a smaller proportion. The drag due to lift constitutes nearly 60% of the total drag of the baseline. As explained, mostly the lift-induced drag D_i is reduced in the optimized design. Increasing the span also reduces the wave drag D_w as it also has an inverse square proportionality to span because it is a drag due to lift. The balance between increased span, more tapering, and root thickness increases keeps the profile drag nearly the same between the optimized and baseline.

Though these appendages were optimized with no dynamic constraints, we analyze their dynamic performance to understand what happens when one neglects dynamic performance in design optimization. Figure 11 plots the evolution of the dimensional eigenvalues of the hydroelastic modes across the flutter speed sweep in the complex plane. The flutter inception speed of the statically optimized foil significantly drops to about 14 m/s for mode 1. Mode 3 of ‘opt1’ also becomes unstable later at 22 m/s, but the lower critical speed is the important one.

We see that the frequency of mode 1 of the ‘opt1’ foil are lower than the baseline throughout the speed sweep primarily due to the increased span and tapering. It eventually flutters at 4.2 Hz. The hydroelastic mode shape at

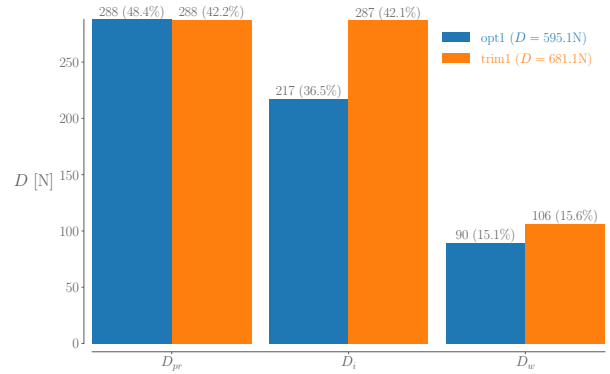


Figure 10: Drag breakdown between opt1 and the baseline (orange) composite foils. Most reductions are in the drag due to lift ($D_i + D_w$)

the critical speed of 14 m/s is shown in Figure 11. It is a mix of twisting and bending shapes resulting from material anisotropy and other sources of bend-twist coupling such as the offset in c.g. from the e.a..

When we turn on the free surface model for the flutter analysis, we obtain the root-locus diagram in Figure 12. We see that ‘opt1-fs’ has marginally increased frequencies of the hydroelastic modes compared to ‘opt1’ because of the added mass corrections and reduced $c_{\ell\alpha}$ ’s. There is minimal impact, but the effect is that the flutter speed increases by hundredths of a meter-per-second, at least for this particular foil at these conditions. This is in agreement with the literature [2]. Considering the quasi-steady free surface effect in the flutter analysis would allow for designs that are less conservative than using the unbounded fluid assumption.

The results of the dynamic analyses are significant because this demonstrates that under a static-only hydroelastic design optimization, the optimized design is dynamically unsafe. We need dynamic constraints in our

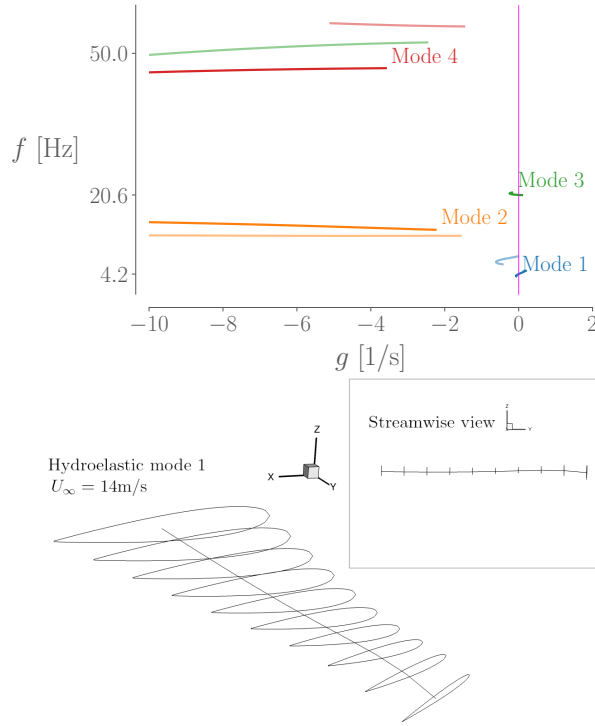


Figure 11: Root-loci of ‘opt1’ versus baseline (faded lines) and the hydroelastic mode shape of ‘opt1’ at the flutter inception speed. The statically optimized foil has flutter instability of mode 1 around 14 m/s when the pole crosses into the right half plane.

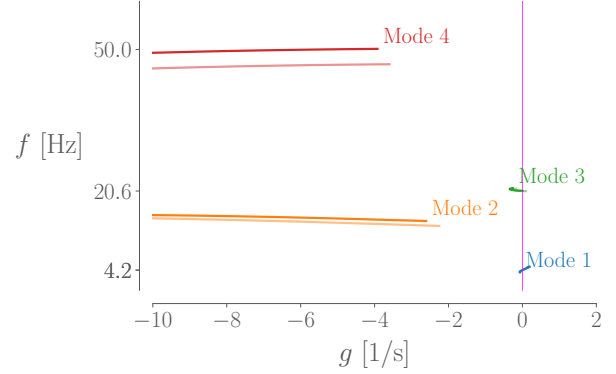


Figure 12: Root-loci of the opt1-fs versus opt1 (faded lines). The free surface effect increases resonance frequencies but generally has minimal impact for these conditions.

optimization, hence the ‘opt2’ optimizations presented next.

Static and dynamic

The spanwise distributions of the ‘opt2-fs’ compared to the baseline composite foils are plotted in [Figure 13](#). The first major difference is that ‘opt2-fs’ achieves a nearly elliptical lift distribution instead of the bell-like distribution on the static-only optimized designs. The twist distributions are very different from the static-only optimized designs too. In the static-only optimizations, we saw the ventilation constraint was at its bound, but that is not the case here because the flutter constraint drives variables a different way.

First, the fiber angle θ_f of ‘opt2-fs’ is high enough to maintain sufficient torsion stiffness to delay flutter. Not decreasing the chord distribution also keeps torsion stiffness sufficiently high to delay flutter, even though reducing it would reduce skin friction drag. The increased chord means the c_ℓ easily stays below the critical ventilation inception $c_{\ell_{in}}$. The increased thickness compared to the static-only optimized cases also seems associated with the flutter constraint. The tip bending constraint is not active as a result. Backwards sweep increases hydrodynamic damping so it delays flutter.

[Figure 14](#) tells a similar story to the drag reductions seen in the static-only optimizations, which is that most drag reduction comes from reducing the drag due to lift. However, the ‘opt2-fs’ suffers an increased profile drag penalty in order to satisfy the flutter constraint. There is about a 10% reduction in total drag. In contrast to the static-only optimized cases that achieved nearly 13%

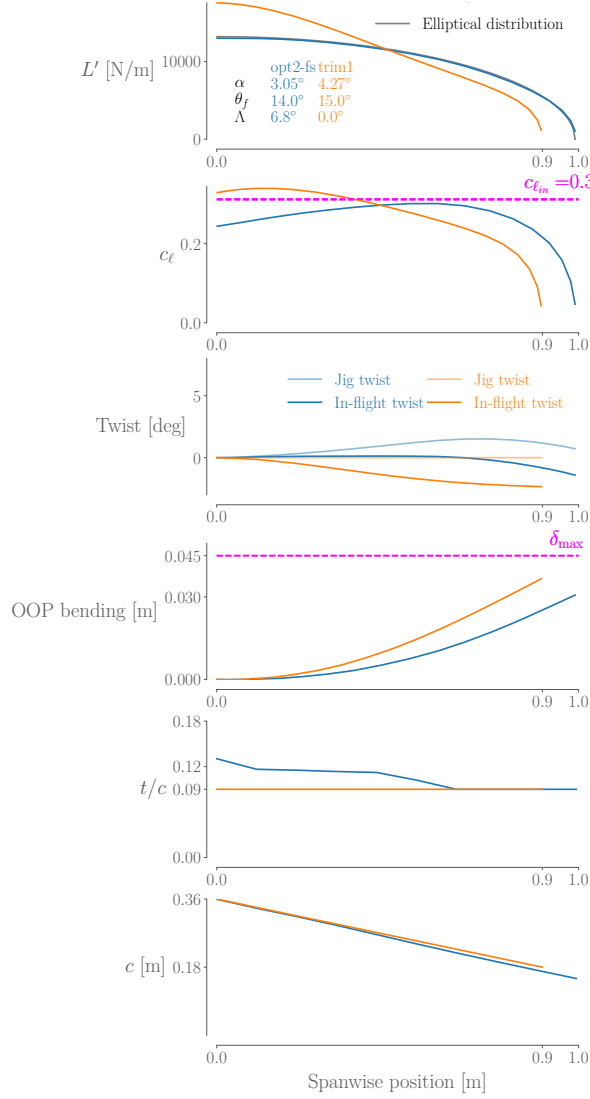


Figure 13: Spanwise attributes of the single point static and dynamic optimized hydrofoil compared to the baseline (orange) at the 17 m/s condition.

drag reduction, there is a drag penalty of about 3% associated with the flutter constraint. This drag penalty in the parasitic drag is a necessary price in increasing the rigidity of the structure to avoid flutter.

Gray et al. [29] and numerous others have observed this drag penalty in subsonic aeroelastic optimizations. The state-of-the-art flutter constrained aeroelastic optimizations use higher fidelity RANS CFD and built-up FEM then condensed to a reduced-order dynamic aeroelastic model [29, 40]. These simulations need to be performed on high-performance computing clusters using parallel computing. Thus, it is significant that we are able to capture the drag and flutter suppression trade with only reduced-order models.

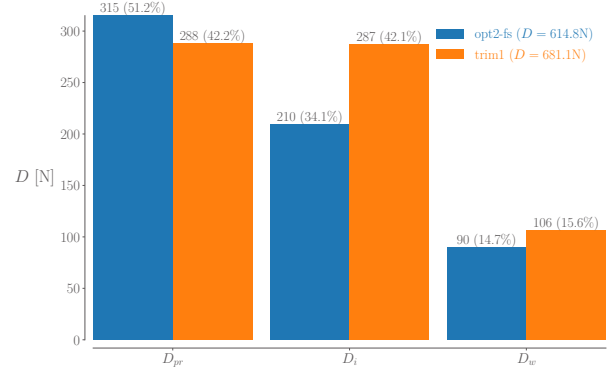


Figure 14: Drag breakdown of the flutter-constrained design ‘opt2-fs’ compared to the baseline (orange).

Figure 15 plots the root-loci of ‘opt2-fs’ compared to the baseline. The design pushes the bounds of the flutter constraint on mode 1 but remains feasible.

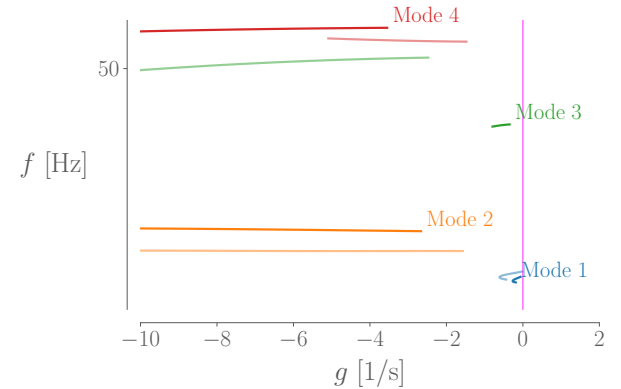


Figure 15: Root-locus diagram of the baseline (faded lines) versus ‘opt2-fs’.

So far, the analyses on designs suggest that consider-

ing the free surface allows for less conservative designs that can push the bounds on constraints. Another set of static and dynamic optimizations using the unbounded fluid assumption correspond to the ‘opt2’, which we compare against the ‘opt2-fs’ results we presented. We want to understand how much the free surface effect impacts the static and dynamic optimization.

In Figure 16, we compare the spanwise distributions of the static and dynamic optimization with and without the free surface model. Many of the design variables are similar; the distribution of thickness-to-chord ratio is the biggest difference. The model without the free surface effect ‘opt2’ has a noticeably higher t/c distribution in-board. This is expected given that the free surface effect tends to raise the flutter speed. As such, neglecting this effect results in an optimized design that has a more robust structure. The t/c distribution seems to be the most significant change when considering the free surface effect, though there are slight differences in the optimized twist distributions.

The differences in twist distributions are side effects of the t/c distribution because the jig twist distributions between ‘opt2’ and ‘opt2-fs’ are nearly identical. The spanwise lift distribution deviates from the ideal as a result with a little too much lift outboard, so ‘opt2’ will have more drag due to lift. This is an interesting feature because there appears to be no constraint or design variable bound stopping the optimizer from modifying the jig twist of ‘opt2’ to achieve the elliptical distribution. Such modifications would not violate the ventilation constraint. This feature may be an artifact of numerical precision or noise from the reduced-order model, optimality tolerance, or the presence of a local minima. From a practical perspective though, these are very small differences that do not mean much in preliminary design. They could be refined at a later stage.

Figure 17 compares the drag build-up between the two designs and shows that ‘opt2’ has more drag than ‘opt2-fs’ in all categories. Compared to each other, ‘opt2-fs’ has around 1.5% more reduction in total drag than ‘opt2’ (see Table 6). The ‘opt2’ has more profile drag because it has more thickness. It has more lift-induced drag primarily because the spanwise lift distribution deviates slightly more than ‘opt2-fs’ from elliptical as it has slightly more lift outboard. The wave drag model does not depend on the spanwise distribution, so we found that the slight increase in wave drag of ‘opt2’ is because it produces a little more lift than ‘opt-fs’, but within the limits of the lift constraints we set. The lift-induced drag is slightly higher because of this effect as well. The wave drag differences are not significant from a design standpoint in the sense that the optimizer is not teaching us a clever design technique to reduce wave drag. The gen-

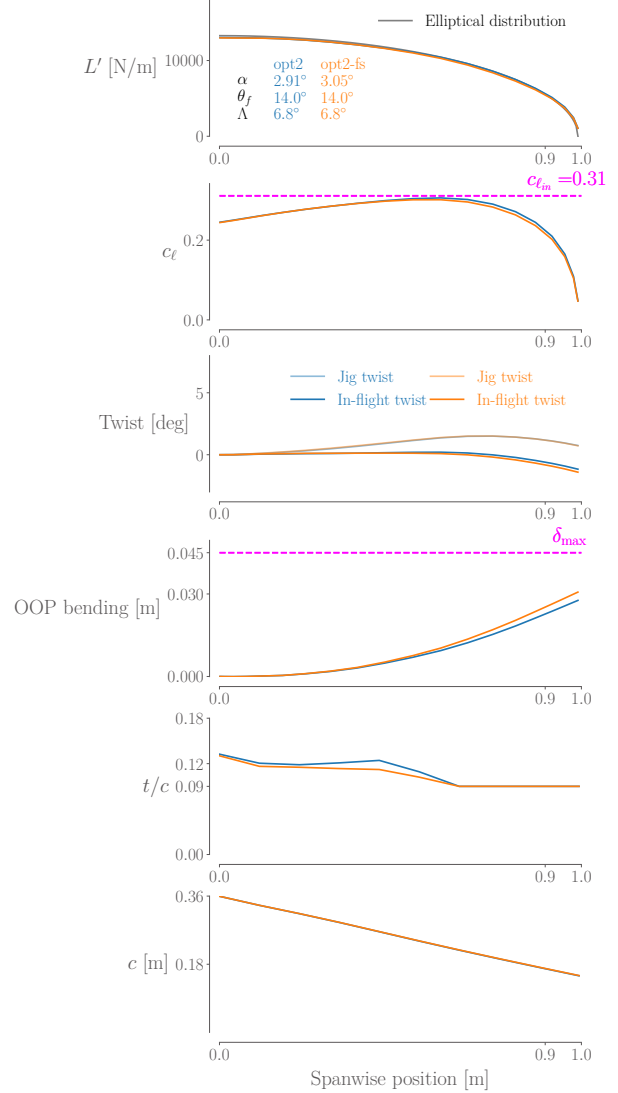


Figure 16: Spanwise attributes of the static and dynamic optimized foils with (‘opt2-fs’ in orange) and without (‘opt2’) consideration for free surface effects during the optimization.

eral conclusion is by considering the free surface effect in a flutter-constrained optimization, one can produce designs with lower profile drag.

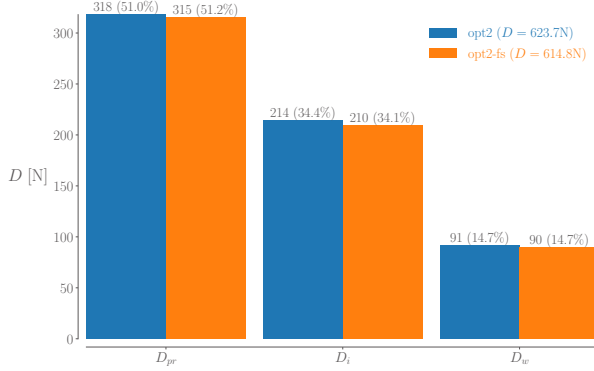


Figure 17: Drag breakdown of the ‘opt2’ and ‘opt2-fs’ designs. Optimization achieves a lower drag design when considering the free surface effect.

The root-loci between ‘opt2’ and ‘opt2-fs’ do not display significant differences that teach us something new so they are not shown. They only showed that the ‘opt2-fs’ design has slightly higher resonance frequencies despite marginally lower structural thicknesses because the free surface effects dominate. We already displayed the free surface effect on the eigenvalue evolution in Figure 12. Capturing the change in resonance frequencies may be important if lock-in and resonance need to be avoided.

Multipoint static and dynamic optimization

Performing single point optimizations means the designs are performant at one particular condition. The performance of single point designs at other speeds or loadings tends to deteriorate [22]. For this reason, we conduct three point design optimization using the conditions from Table 4.

The resulting drag of the foils is summarized in Table 7. Optimization achieves decent reductions in the weighted drag objective of over 6%. There is no noticeable difference in drag reduction whether a free surface is considered or not. The designs in either case ended up identical hence the ‘opt3’ case is not plotted for brevity.

Figure 18 compares the spanwise attributes of ‘opt3-fs’ to the baseline. The optimized design is similar but different from the previous single point designs. The span goes to its maximum to reduce drag due to lift. Unlike the flutter-constrained optimizations (opt2 family), the spanwise lift distribution is not elliptical. This is be-

Table 7: Drag of multipoint optimized designs with percent reductions compared to the baseline

Parameter	opt3-fs	opt3	Baseline	Units
$\sum_i^{npts} wt_i \times D$	539 (-6.4%)	539 (-6.4%)	576	N
$\sum_i^{npts} D$	1719 (-6.8%)	1719 (-6.8%)	1844	N

cause the high C_L condition only has a 10% weight in the drag objective so reducing parasitic drag is prioritized. The spanwise lift distributions look more similar to the static-only optimizations (opt1 family). These foils have bell-like lift distributions and their c_ℓ distributions are up against the ventilation limit at the p3 condition as a result of reduced chord.

Figure 19 shows the drag breakdown of the multipoint design. The parasitic drag is over 60% of the total drag when considering the three design points. We see that all categories of drag are reduced compared to the baseline. The tapering reduces skin friction drag overall despite the conflict with increasing span. The increased span reduces the lift-induced and wave drag. It is likely that if the low-speed, higher lift condition were more heavily weighted in the drag objective, we would see lift distributions closer to elliptical.

The fiber angle is much closer to 0° than the previous sets of optimizations, so this means bending stiffness is important. We see that for the p3 condition, ‘opt3-fs’ is at the tip deflection bound. Any reduction in bending stiffness would violate this constraint. The value of $\theta_f = 4.5^\circ$ provides slight material nose-down bend-twist coupling. There is only slight twist in its deflected states shown in Figure 18.

Interestingly, there is no sweep despite this being a multipoint design. The addition of sweep here would lead to hydrodynamic inefficiencies with more washout and increase lift-induced drag. Because the foil is not trying to achieve an elliptical lift distribution at any of the points (which is partially caused by the ventilation constraint), sweep is not a design variable that can help reduce drag. Backward sweep could increase damping to delay flutter, but the optimizer has found a sufficiently damped design such that it does not need sweep.

The root-loci of ‘opt3-fs’ versus the baseline are in Figure 20. The optimized foil avoids flutter, but mode 1 is extremely lightly damped across the entire speed envelope in comparison to the baseline. This can be problematic when subjected to wave-induced loads that tend to be lower frequency. Ocean wave periods are on the order of 10 seconds, but they can get as low as 3–5 seconds in the Great Lakes [70, Ch. 8].

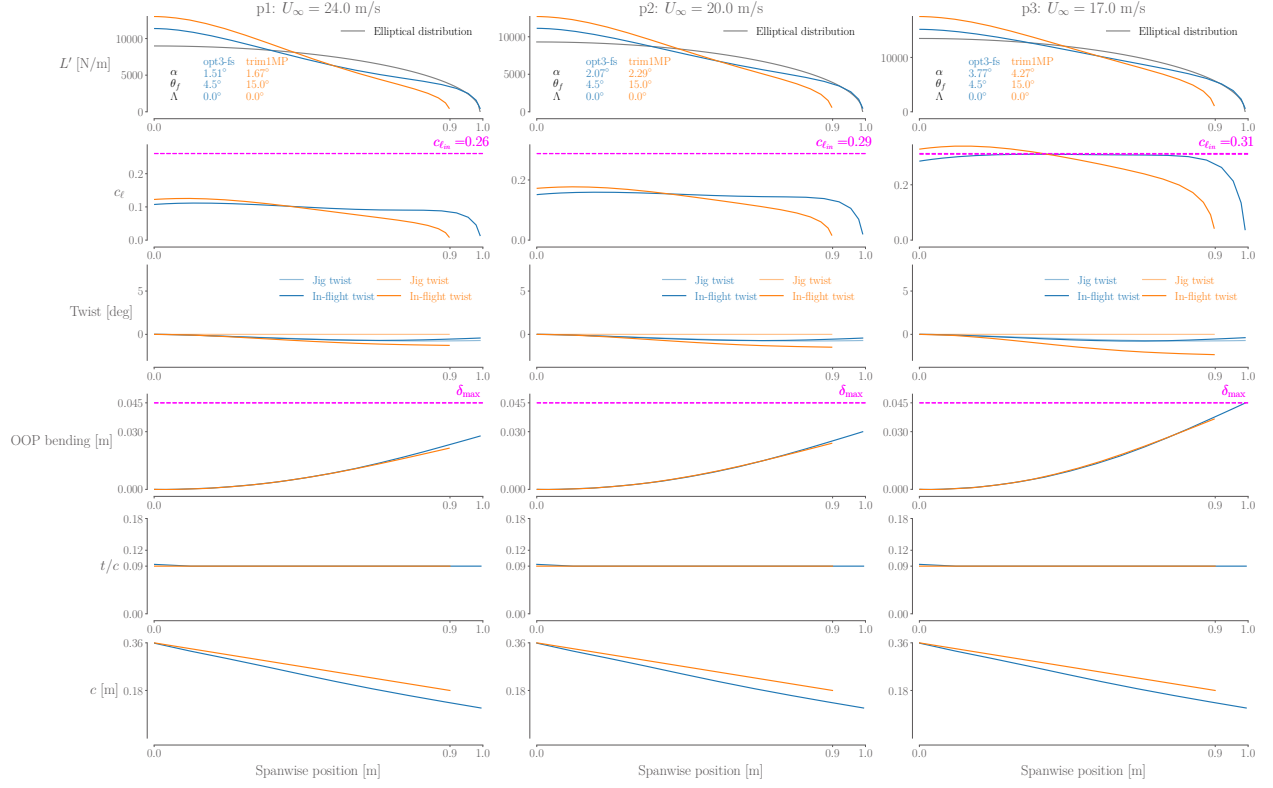


Figure 18: Spanwise attributes of the multipoint static and dynamic optimized foil 'opt3-fs' (blue) compared to the baseline.

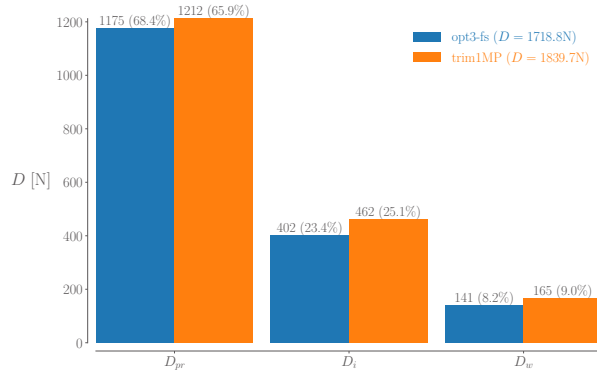


Figure 19: Drag breakdown of the multipoint optimized foil versus the baseline (orange).

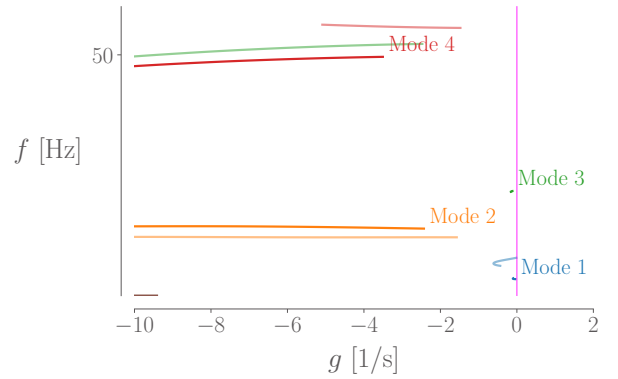


Figure 20: Root-loci of the 'opt3-fs' (solid lines) versus the baseline.

Conclusions

We created a framework for enabling scalable and generic composite marine appendage design optimization to consider flutter and ventilation constraints for the first time in the published literature. All the design variables, geometric and structural, have interplay and impact the design of an optimal and feasible composite hydrofoil; the optimization methodology presented here allows us to explore the design space more efficiently. Through several studies, we used the methodology to learn about hydroelastic design of composite hydrofoils.

We used this framework to successfully minimize the total drag (between 6–14% reduction) of a cantilevered composite hydrofoil subject to constraints. We make these design recommendations based on our studies:

- To reduce the total drag, increasing the span while reducing local chord is a higher priority than achieving an elliptical lift distribution when there are strict constraints.
- Optimizing with no flutter constraint results in an unsafe design so we need this constraint, but there is a drag penalty associated with satisfying the flutter constraint.
- Considering the quasi-steady free surface effect in design can result in minor parasitic drag reductions because the structure can be thinned out more.

These recommendations apply to several hydrofoil applications such as high-performance racing yachts and high-speed surface craft.

There are several areas of future exploration. One possibility is to consider different depth-to-chord ratios in the design points to observe how free surface proximity impacts the design and if there are particular situations where it matters more or less.

Though the dynamic constraints use numerous techniques to reduce cost, we observed some instances where the reverse AD derivative computation for the flutter cost function used large amounts of memory (up to 50GB of RAM). The desktop computer on which we ran simulations had 64GB of RAM so this did not cause failures. However, future work should investigate methods to reduce the memory usage so these types of optimizations could be conducted on a decent laptop rather than a desktop. Through surveying other Julia codes, we believe the primary culprit is the data types we used for the reverse AD package `Zygote.jl`. More specifically, we use buffer data types during the frequency and speed loops. Refactoring of the source code to work with `ReverseDiff.jl` and `Mooncake.jl` are cited to be more efficient.

Lastly, most of the reduced-order models in DCfoil have been independently validated [55, 56] for simpler cases, but it would be valuable to experimentally validate an optimized design. We have an ongoing effort to obtain cavitation tunnel and modal test data on an optimized CFRP hydrofoil at the Australia Maritime College that would help increase our confidence in using this model for design.

This methodology using reduced-order models and gradient-based optimization is valuable to the preliminary design of high-performance composite hydrofoils, especially if ventilation and flutter are problems. It could be incorporated into practical design workflows to determine initial designs to pursue in the detail design phase to help save time and resources.

Bibliography

- [1] M. Abramowitz and I. A. Stegun. *Handbook of mathematical functions with formulas, graphs, and mathematical tables*, volume 55. US Government printing office, 1968.
- [2] H. N. Abramson. Hydroelasticity review of hydrofoil flutter. *Applied Mechanics Reviews*, 22(2), 1969.
- [3] D. T. Akcabay and Y. L. Young. Steady and dynamic hydroelastic behavior of composite lifting surfaces. *Composite Structures*, 227:111240, November 2019. doi:[10.1016/j.compstruct.2019.111240](https://doi.org/10.1016/j.compstruct.2019.111240).
- [4] D. T. Akcabay and Y. L. Young. Material anisotropy and sweep effects on the hydroelastic response of lifting surfaces. *Composite Structures*, 242:112140, 2020. ISSN 0263-8223. doi:[10.1016/j.compstruct.2020.112140](https://doi.org/10.1016/j.compstruct.2020.112140).
- [5] E. Baird, C. Squires, and R. Caporali. Investigation of hydrofoil flutter-final report. *Grumman Aircraft Engineering Corporation Report DA*, 10: 480–3, 1962.
- [6] R. Balze, H. Devaux, and L. Jézéquel. Study of a hydroelastic instability phenomenon: flutter of racing yacht keels. In *Engineering Systems Design and Analysis*, volume 44878, pages 391–401. American Society of Mechanical Engineers, 2012.
- [7] P. K. Besch and Y.-N. Liu. Flutter and divergence characteristics of four low mass ratio hydrofoils. Technical Report 3410, 1971.
- [8] P. K. Besch and Y.-N. Liu. Bending flutter and torsional flutter of flexible hydrofoil struts. In *9th Symposium on Naval Hydrodynamics*, pages 343–400, 1972.
- [9] P. K. Besch and Y.-N. Liu. Hydroelastic design of subcavitating and cavitating hydrofoil strut systems. Technical report, Naval Ship Research and Development Center, Bethesda, Maryland, U.S.A., 1974.
- [10] P. K. Besch and E. P. Rood. A parametric survey of hydrofoil strut flutter. Technical Report 50, 1976.
- [11] R. L. Bisplinghoff, H. Ashley, and R. L. Halfman. *Aeroelasticity*. Courier Corporation, 2013.
- [12] R. D. Blevins. *Flow-induced Vibration*. Krieger Publishing Company, 2nd edition, 2001. ISBN 9781575241838.
- [13] C. E. Brennen. A review of added mass and fluid inertial forces. Technical Report CR 82.010, Naval Civil Engineering Laboratory, January 1982.
- [14] J. P. Breslin. Application of ship-wave theory to the hydrofoil of finite span. *Journal of Ship Research*, 1(02):27–55, 04 1957. ISSN 0022-4502. doi:[10.5957/jsr.1957.1.2.27](https://doi.org/10.5957/jsr.1957.1.2.27).
- [15] J. S. Carlton. *Marine Propellers and Propulsion*. Butterworth-Heinemann, 4th edition, 2018.
- [16] E. J. Chae and Y. L. Young. Influence of spanwise flexibility on steady and dynamic responses of airfoils vs hydrofoils. *Physics of Fluids*, 33(6): 067124, 2021. doi:[10.1063/5.0052192](https://doi.org/10.1063/5.0052192).
- [17] E. J. Chae, D. T. Akcabay, and Y. L. Young. Dynamic response and stability of a flapping foil in a dense and viscous fluid. *Physics of Fluids*, 25(10): 104106, 2013. doi:[10.1063/1.4825136](https://doi.org/10.1063/1.4825136).
- [18] E. J. Chae, D. T. Akcabay, and Y. L. Young. Influence of flow-induced bend–twist coupling on the natural vibration responses of flexible hydrofoils. *Journal of Fluids and Structures*, 69:323–340, 2017. doi:[10.1016/j.jfluidstructs.2016.12.008](https://doi.org/10.1016/j.jfluidstructs.2016.12.008).
- [19] A. Champneys. Dynamics of Parametric Excitation. In *Mathematics of Complexity and Dynamical Systems*, pages 183–204. Springer New York, New York, NY, 2012.
- [20] A. Damley-Strnad, C. M. Harwood, and Y. L. Young. Hydrodynamic performance and hysteresis response of hydrofoils in ventilated flows. In *Sixth International Symposium on Marine Propellers*, Rome, Italy, 2019.
- [21] E. H. Dowell. *A Modern Course in Aeroelasticity*. Springer International Publishing, 2022. ISBN 9783030742362. doi:[10.1007/978-3-030-74236-2](https://doi.org/10.1007/978-3-030-74236-2).

- [22] M. Drela. *Frontiers of Computational Fluid Dynamics*, chapter Pros and Cons of Airfoil Optimization, pages 363–381. World Scientific, Singapore, November 1998. ISBN 978-981-02-3707-3. doi:[10.1142/9789810237073_0019](https://doi.org/10.1142/9789810237073_0019).
- [23] O. M. Faltinsen. *Hydrodynamics of high-speed marine vehicles*. Cambridge University Press, 2006. ISBN 9780511546068. doi:[10.1017/CBO9780511546068](https://doi.org/10.1017/CBO9780511546068).
- [24] N. Garg, G. K. W. Kenway, J. R. R. A. Martins, and Y. L. Young. High-fidelity multipoint hydrostructural optimization of a 3-D hydrofoil. *Journal of Fluids and Structures*, 71:15–39, May 2017. doi:[10.1016/j.jfluidstructs.2017.02.001](https://doi.org/10.1016/j.jfluidstructs.2017.02.001).
- [25] P. E. Gill, W. Murray, and M. A. Saunders. SNOPT: An SQP algorithm for large-scale constrained optimization. *SIAM Journal of Optimization*, 12(4):979–1006, 2002. doi:[10.1137/S1052623499350013](https://doi.org/10.1137/S1052623499350013).
- [26] P. E. Gill, W. Murray, and M. A. Saunders. SNOPT: An SQP algorithm for large-scale constrained optimization. *SIAM Review*, 47(1):99–131, 2005. doi:[10.1137/S0036144504446096](https://doi.org/10.1137/S0036144504446096).
- [27] P. E. Gill, W. Murray, and M. A. Saunders. *User’s Guide for SNOPT Version 7: Software for Large-Scale Nonlinear Programming*. Systems Optimization Laboratory, Stanford University, California, 94305-4023, 2007. Technical Report.
- [28] T. Golla, G. J. Kennedy, and C. Riso. Sliding-window matrix pencil method for design optimization with limit-cycle oscillation constraints. *AIAA Journal*, 62(11):4170–4188, 2024. doi:[10.2514/1.J064005](https://doi.org/10.2514/1.J064005).
- [29] A. C. Gray, C. Riso, E. Jonsson, J. R. R. A. Martins, and C. E. S. Cesnik. High-fidelity aerostructural optimization with a geometrically nonlinear flutter constraint. *AIAA Journal*, 61(6):2430–2443, April 2023. doi:[10.2514/1.J062127](https://doi.org/10.2514/1.J062127).
- [30] J. S. Gray, J. T. Hwang, J. R. R. A. Martins, K. T. Moore, and B. A. Naylor. OpenMDAO: An open-source framework for multidisciplinary design, analysis, and optimization. *Structural and Multidisciplinary Optimization*, 59(4):1075–1104, April 2019. doi:[10.1007/s00158-019-02211-z](https://doi.org/10.1007/s00158-019-02211-z).
- [31] H. M. Hajdik, A. Yildirim, E. Wu, B. J. Brelje, S. Seraj, M. Mangano, J. L. Anibal, E. Jonsson, E. J. Adler, C. A. Mader, G. K. W. Kenway, and J. R. R. A. Martins. pyGeo: A geometry package for multidisciplinary design optimization. *Journal of Open Source Software*, 8(87):5319, July 2023. doi:[10.21105/joss.05319](https://doi.org/10.21105/joss.05319).
- [32] C. M. Harwood, Y. L. Young, and S. L. Ceccio. Ventilated cavities on a surface-piercing hydrofoil at moderate froude numbers: cavity formation, elimination and stability. *Journal of Fluid Mechanics*, 800:5–56, 2016. doi:[10.1017/jfm.2016.373](https://doi.org/10.1017/jfm.2016.373).
- [33] H. J. Hassig. An approximate true damping solution of the flutter equation by determinant iteration. *Journal of Aircraft*, 8(11):885–889, 1971. doi:[10.2514/3.44311](https://doi.org/10.2514/3.44311).
- [34] D. F. Hunsaker and W. Phillips. Ludwig Prandtl’s 1933 paper concerning wings for minimum induced drag, translation and commentary. In *AIAA Scitech 2020 Forum*, page 0644, 2020. doi:[10.2514/6.2020-0644](https://doi.org/10.2514/6.2020-0644).
- [35] J. T. Hwang and J. R. R. A. Martins. A computational architecture for coupling heterogeneous numerical models and computing coupled derivatives. *ACM Transactions on Mathematical Software*, 44(4):Article 37, June 2018. doi:[10.1145/3182393](https://doi.org/10.1145/3182393).
- [36] D. A. Jewell. A note on hydroelasticity. *Journal of Ship Research*, 4(01):9–29, 1960. doi:[10.5957/jsr.1960.4.1.9](https://doi.org/10.5957/jsr.1960.4.1.9).
- [37] R. S. Johnson. Prediction of lift and cavitation characteristics of hydrofoil-strut arrays. *Marine Technology and SNAME News*, 2(01):57–69, 1965. doi:[10.5957/mt.1965.2.1.57](https://doi.org/10.5957/mt.1965.2.1.57).
- [38] E. Jonsson, G. K. W. Kenway, G. J. Kennedy, and J. R. R. A. Martins. Development of flutter constraints for high-fidelity aerostructural optimization. In *18th AIAA/ISSMO Multidisciplinary Analysis and Optimization Conference*, Denver, CO, June 2017. doi:[10.2514/6.2017-4455](https://doi.org/10.2514/6.2017-4455).
- [39] E. Jonsson, C. A. Mader, G. J. Kennedy, and J. R. R. A. Martins. Computational modeling of flutter constraint for high-fidelity aerostructural optimization. In *2019 AIAA/ASCE/AHS/ASC Structures, Structural Dynamics, and Materials Conference*, San Diego, CA, January 2019. American Institute of Aeronautics and Astronautics. doi:[10.2514/6.2019-2354](https://doi.org/10.2514/6.2019-2354).
- [40] E. Jonsson, C. Riso, B. B. Monteiro, A. C. Gray, J. R. R. A. Martins, and C. E. S. Cesnik. High-fidelity gradient-based wing structural optimization including geometrically nonlinear flutter con-

- straint. *AIAA Journal*, 61(7):3045–3061, July 2023. doi:[10.2514/1.J061575](https://doi.org/10.2514/1.J061575).
- [41] W. Karush. Minima of functions of several variables with inequalities as side constraints. Master’s thesis, Chicago, IL, 1939. URL <https://catalog.lib.uchicago.edu/vufind/Record/4111654>.
- [42] G. K. Kenway, G. J. Kennedy, and J. R. R. A. Martins. A CAD-free approach to high-fidelity aerostructural optimization. In *Proceedings of the 13th AIAA/ISSMO Multidisciplinary Analysis Optimization Conference*, number AIAA 2010-9231, Fort Worth, TX, September 2010. doi:[10.2514/6.2010-9231](https://doi.org/10.2514/6.2010-9231).
- [43] G. Kreisselmeier and R. Steinhauser. Systematic control design by optimizing a vector performance index. In *International Federation of Active Controls Symposium on Computer-Aided Design of Control Systems, Zurich, Switzerland*, 1979. doi:[10.1016/S1474-6670\(17\)65584-8](https://doi.org/10.1016/S1474-6670(17)65584-8).
- [44] I. M. Kroo. Drag due to lift: Concepts for prediction and reduction. *Annual Review of Fluid Mechanics*, 33:587–617, November 2001. doi:[10.1146/annurev.fluid.33.1.587](https://doi.org/10.1146/annurev.fluid.33.1.587).
- [45] H. W. Kuhn and A. W. Tucker. *Nonlinear programming*, pages 481–492. 1951.
- [46] M. W. Kutta. Auftriebskräfte in strömenden flüssigkeiten. *Illustrierte Aeronautische Mitteilungen*, 6:133–135, 1902.
- [47] H. Lamb. *Hydrodynamics*. Dover Publications, 6th edition, 1932.
- [48] A. B. Lambe and J. R. R. A. Martins. Extensions to the design structure matrix for the description of multidisciplinary design, analysis, and optimization processes. *Structural and Multidisciplinary Optimization*, 46(2):273–284, August 2012. doi:[10.1007/s00158-012-0763-y](https://doi.org/10.1007/s00158-012-0763-y).
- [49] Y. Liao, J. R. R. A. Martins, and Y. L. Young. Sweep and anisotropy effects on the viscous hydroelastic response of composite hydrofoils. *Composite Structures*, 230:111471, December 2019. doi:[10.1016/j.compstruct.2019.111471](https://doi.org/10.1016/j.compstruct.2019.111471).
- [50] Y. Liao, J. R. R. A. Martins, and Y. L. Young. 3-D high-fidelity hydrostructural optimization of cavitation-free composite lifting surfaces. *Composite Structures*, 268:113937, July 2021. doi:[10.1016/j.compstruct.2021.113937](https://doi.org/10.1016/j.compstruct.2021.113937).
- [51] Y. Liao, J. R. R. A. Martins, and Y. L. Young. Hydrostructural optimization of single-layer and multi-layer composite lifting surfaces. *Composite Structures*, 307:116650, March 2023. doi:[10.1016/j.compstruct.2022.116650](https://doi.org/10.1016/j.compstruct.2022.116650).
- [52] Y.-N. Liu and P. K. Besch. Hydrofoil flutter analysis, using a modified strip theory. Technical Report 3624, Naval Ship Research and Development Center, Washington, D.C., July 1971.
- [53] J. R. R. A. Martins and J. T. Hwang. Review and unification of methods for computing derivatives of multidisciplinary computational models. *AIAA Journal*, 51(11):2582–2599, November 2013. doi:[10.2514/1.J052184](https://doi.org/10.2514/1.J052184).
- [54] J. N. Newman. *Marine hydrodynamics*. The MIT press, 2018.
- [55] G. W. Ng, E. Jonsson, S. He, and J. R. Martins. Dynamic hydroelasticity of composite appendages with reverse-mode algorithmic differentiation. *Composite Structures*, 2024. doi:[10.1016/j.compstruct.2024.118367](https://doi.org/10.1016/j.compstruct.2024.118367).
- [56] G. W. Ng, E. Jonsson, Y. Liao, S. He, and J. R. Martins. Static hydroelastic study of composite t-foils with beam and lifting line models. In *International Marine Design Conference*, 2024. doi:[10.59490/imdc.2024.900](https://doi.org/10.59490/imdc.2024.900).
- [57] G. W. Ng, Y. Liao, A. Yildirim, and J. R. R. A. Martins. Hydrostructural optimization of subcavitating cambered and symmetric composite foils. *Composite Structures*, 351:118545, January 2025. doi:[10.1016/j.compstruct.2024.118545](https://doi.org/10.1016/j.compstruct.2024.118545).
- [58] W. Phillips and D. Snyder. Modern adaptation of prandtl’s classic lifting-line theory. *Journal of Aircraft*, 37(4):662–670, 2000.
- [59] L. Prandtl. Induced drag of multiplanes. Technical Note NACA-TN-182, NACA, February 1924.
- [60] L. Prandtl. Über Tragflügel kleinsten induzierten Widerstandes. *Zeitschrift für Flugtechnik und Motorluftschiffahrt*, pages 305–306, 1933. URL https://link.springer.com/chapter/10.1007/978-3-662-11836-8_40.
- [61] D. P. Raymer. *Aircraft Design: A Conceptual Approach*. AIAA, Reston, VA, 5th edition, 2012.
- [62] J. T. Reid and D. F. Hunsaker. General approach to lifting-line theory, applied to wings with

- sweep. *Journal of Aircraft*, 58(2):334–346, 2021. doi:[10.2514/1.C035994](https://doi.org/10.2514/1.C035994).
- [63] M. Sacher, M. Durand, É. Berrini, F. Hauville, R. Duval, O. Le Maître, and J.-A. Astolfi. Flexible hydrofoil optimization for the 35th America’s Cup with constrained EGO method. *Ocean Engineering*, 157:62–72, June 2018. ISSN 0029-8018. doi:[10.1016/j.oceaneng.2018.03.047](https://doi.org/10.1016/j.oceaneng.2018.03.047).
- [64] W. R. Sears. Some aspects of non-stationary airfoil theory and its practical application. *Journal of the Aeronautical Sciences*, 8(3):104–108, 1941. doi:[10.2514/8.10655](https://doi.org/10.2514/8.10655).
- [65] P. Swales, A. Wright, R. McGregor, and R. S. Rothblum. The mechanism of ventilation inception on surface piercing foils. *Journal of Mechanical Engineering Science*, 16(1):18–24, 1974. doi:[10.1243/JMES_JOUR_1974.016.005.02](https://doi.org/10.1243/JMES_JOUR_1974.016.005.02).
- [66] R. Tannenber, S. R. Turnock, K. Hochkirch, and S. W. Boyd. VPP driven parametric design of ac75 hydrofoils. *Journal of Sailing Technology*, 8(01): 161–182, 2023. doi:[10.5957/jst/2023.8.9.161](https://doi.org/10.5957/jst/2023.8.9.161).
- [67] T. Theodorsen. General theory of aerodynamic instability and the mechanism of flutter. Technical Report Rept. 496, NACA, May 1934.
- [68] G. D. Thiart. Numerical lifting line theory for a hydrofoil near a free surface. *R&D Journal*, 10: 18–23, 1994.
- [69] E. Torenbeek. *Synthesis of Subsonic Airplane Design*. Delft University Press and Kluwer Academic Publishers, Delft, NL, 6th edition, 1990.
- [70] A. W. Troesch. *Introduction to Marine Dynamics*. Cambridge University Press, 2024. ISBN 9781009418096. doi:[10.1017/9781009418065](https://doi.org/10.1017/9781009418065).
- [71] F. Van Walree. *Computational methods for hydrofoil craft in steady and unsteady flow*. PhD thesis, Technical University of Delft, 1999.
- [72] L. H. van Zyl. Use of eigenvectors in the solution of the flutter equation. *Journal of Aircraft*, 30(4):553–554, July 1993. ISSN 0021-8669. doi:[10.2514/3.46380](https://doi.org/10.2514/3.46380). URL <http://dx.doi.org/10.2514/3.46380>.
- [73] L. H. van Zyl. Aeroelastic divergence and aerodynamic lag roots. *Journal of Aircraft*, 38(3):586–588, May 2001. ISSN 0021-8669. doi:[10.2514/2.2806](https://doi.org/10.2514/2.2806). URL <http://dx.doi.org/10.2514/2.2806>.
- [74] V. Z. Vlasov. *Thin-walled elastic beams*. US Department of Commerce, 2nd edition, 1961.
- [75] S. Volpi, M. Diez, and F. Stern. *Multidisciplinary Design Optimization of a 3D Composite Hydrofoil via Variable Accuracy Architecture*. American Institute of Aeronautics and Astronautics, 2018/07/23 2018. doi:[10.2514/6.2018-4173](https://doi.org/10.2514/6.2018-4173).
- [76] W. S. Vorus. *Principles of Naval Architecture Series: Vibration*. The Society of Naval Architects and Marine Engineers (SNAME), 2010.
- [77] K. L. Wadlin, C. L. Shuford Jr, and J. R. McGehee. A theoretical and experimental investigation of the lift and drag characteristics of hydrofoils at subcritical and supercritical speeds. Technical report, 1955.
- [78] E. Wu, G. Kenway, C. A. Mader, J. Jasa, and J. R. R. A. Martins. pyOptSparse: a Python framework for large-scale constrained nonlinear optimization of sparse systems. *Journal of Open Source Software*, 5(54):2564, October 2020. doi:[10.21105/joss.02564](https://doi.org/10.21105/joss.02564).
- [79] E. C. Yates. Modified-strip-analysis method for predicting wing flutter at subsonic to hypersonic speeds. *Journal of Aircraft*, 3(1):25–29, 1966. ISSN 15333868. doi:[10.2514/3.43702](https://doi.org/10.2514/3.43702).
- [80] E. C. Yates. Flutter prediction at low mass-density ratios with application to the finite-span noncavitating hydrofoil. In *3rd Marine Systems and ASW Meeting*, number 68-472, 1968.
- [81] Y. Young, T. Wright, H. Yoon, and C. Harwood. Dynamic hydroelastic response of a surface-piercing strut in waves and ventilated flows. *Journal of Fluids and Structures*, 94:102899, April 2020. ISSN 08899746. doi:[10.1016/j.jfluidstructs.2020.102899](https://doi.org/10.1016/j.jfluidstructs.2020.102899).
- [82] Y. L. Young, C. M. Harwood, M. F. Montero, J. C. Ward, and S. L. Ceccio. Ventilation of lifting bodies: Review of the physics and discussion of scaling effects. *Applied Mechanics Reviews*, 69(1): 010801, 2017.
- [83] Y. L. Young, T. Wright, H. Yoon, and C. M. Harwood. Dynamic hydroelastic response of a surface-piercing strut in waves and ventilated flows. *Journal of Fluids and Structures*, 94:102899, 2020. ISSN 0889-9746. doi:[10.1016/j.jfluidstructs.2020.102899](https://doi.org/10.1016/j.jfluidstructs.2020.102899).

- [84] Y. L. Young, J. Chang, S. M. Smith, J. A. Vening, B. W. Pearce, and P. A. Brandner. The influence of fluid-structure interaction on cloud cavitation about a stiff hydrofoil. part 3. *Journal of Fluid Mechanics*, 2021. ISSN 14697645.
- [85] Y. L. Young, Z. Valles, I. D. Napoli, F. M. Montero, L. F. Minerva, and C. Harwood. Fixed and control motion response of a surface-piercing hydrofoil in multiphase flow and in waves. In *33rd Symposium on Naval Hydrodynamics*, 2022.
- [86] Y. L. Young, Z. Valles, I. Di Napoli, F. M. Montero, L. F. Minerva, and C. Harwood. Wave effects on the hydroelastic response of a surface-piercing hydrofoil. part 1. fully wetted and ventilated flows. *Journal of Fluid Mechanics*, 963:A37, 2023. doi:[10.1017/jfm.2023.127](https://doi.org/10.1017/jfm.2023.127).
- [87] Y. L. Young, Z. Valles, I. Di Napoli, F. M. Montero, L. F. Minerva, and C. Harwood. Wave effects on the hydroelastic response of a surface-piercing hydrofoil. part 2. cavitating and ventilating flows. *Journal of Fluid Mechanics*, 965:A3, 2023. doi:[10.1017/jfm.2023.254](https://doi.org/10.1017/jfm.2023.254).
- [88] N. E. Zhukovsky. On annexed vortices. *Proceedings of Physics Section of the Natural Science Society*, 13(2):12–25, 1906.

APPENDIX B

2025 Mandles Prize for Hydrofoil Excellence

Approval for Release and Publication

By signing this agreement, the author(s) certify that they have obtained all appropriate approval and clearance for public release which might be required to permit the work to be published. The authors agree to provide objective evidence of such review and approval if requested.

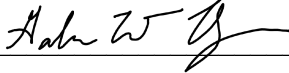
Please indicate acceptance of this agreement by completing the following form:

1. The submitted work is unclassified and all appropriate approvals and releases for publication have been obtained.
2. The work is original and has not previously been published and is not currently being considered for publication elsewhere. (Please indicate any exceptions.)

Project Title: Gradient-based Optimization of Submerged Composite Hydrofoils with Flutter and Ventilation Constraints

School: The University of Michigan

Author(s) name(s), email addresses and signature(s):

 Galen W. Ng, nggw@umich.edu, 

Date 2025-07-05

Faculty Adviser email address and signature: _

jrram@umich.edu

A handwritten signature in black ink, appearing to be 'J. Ram', is written over a horizontal line.

Date: 07/07/2025

* If signed by only one of multiple authors, the signing author certifies that all authors understand and agree to the terms set forth in this agreement.

For questions about any aspect of this agreement, please contact Mark Bebar at:

markbebar334231@gmail.com or Ray Vellinga at: IHSpresident2016@gmail.com

Statement of originality:

To whom it may concern,

I, Joaquim R.R.A. Martins, certify that the work titled “Gradient-based Optimization of Submerged Composite Hydrofoils with Flutter and Ventilation Constraints” was done by the student, Galen W. Ng.

Regards,

A handwritten signature in black ink, appearing to read 'J. Martins', with a stylized flourish at the end.

Joaquim R.R.A. Martins
Pauline M. Sherman Collegiate Professor
Department of Aerospace Engineering
The University of Michigan
jrram@umich.edu